communications earth & environment

ARTICLE

https://doi.org/10.1038/s43247-023-01080-1 OPEN

Evidence for high-frequency oxygenation of Ediacaran shelf seafloor during early evolution of complex life

Liangxuan Jiao[1,2,3], Zhenbing She[2✉], Dominic Papineau[2,4,5,6], Chao Zhang[7,8], Thomas J. Algeo[2,9,10], Matthew S. Dodd[1,2,3], Genming Luo[2], Kenan Cao[2] & Chao Li[1,2,3]

Increasing oxygenation of the early Ediacaran Ocean is thought to have been responsible for the emergence of early animals. Although geochemical studies have suggested periods of oceanic oxygenation in the Ediacaran, direct evidence for seafloor oxygenation has been lacking. Here, we report frequent occurrences of distinctive, sub-millimetric, and early diagenetic pyrite-marcasite rosettes in phosphorites from the lower Ediacaran Doushantuo Formation (Weng'an, South China). They typically consist of a nucleus of framboidal pyrite, a cortex of radiating marcasite blades intergrown with quartz, and a rim of second-generation pyrite, recording partial oxidative dissolution of pyrite and co-precipitation of marcasite and quartz. This inference is further supported by near-zero carbon isotope values of the host dolostone, similarly low sulfur isotope values for pyrite and marcasite, and evident Fe-isotope fractionation between marcasite and pyrite. Collectively, our findings reveal intermittent bottom-water and porewater oxygenation events, providing direct evidence of high-frequency oxygenation of Ediacaran continental shelves.

[1] State Key Laboratory of Oil and Gas Reservoir Geology and Exploitation & Institute of Sedimentary Geology, Chengdu University of Technology, Chengdu, China. [2] State Key Laboratory of Biogeology and Environmental Geology, School of Earth Sciences, China University of Geosciences, Wuhan, China. [3] International Center for Sedimentary Geochemistry and Biogeochemistry Research, Chengdu University of Technology, Chengdu, China. [4] London Centre for Nanotechnology, University College London, London, UK. [5] Department of Earth Sciences, University College London, London, UK. [6] Centre for Planetary Science, University College London and Birkbeck College, London, UK. [7] Department of Geology, Northwest University, Xi'an, China. [8] Institute of Mineralogy, Leibniz University Hannover, Welfengarten 1, Hannover, Germany. [9] State Key Laboratory of Geological Processes and Mineral Resources, China University of Geosciences, Wuhan, China. [10] Department of Geosciences, University of Cincinnati, Cincinnati, OH, USA. ✉email: zbsher@cug.edu.cn

The Ediacaran Period (635–539 Ma) was a crucial time in Earth's history that witnessed profound changes in global climate, marine environment, and biological evolution[1–3], with hypothesized oceanic oxygenation events promoting the rise of animals[4–8]. However, the exact links between oceanic oxygenation and early animal evolution remain in debate, a key reason being the complex redox history of the Ediacaran ocean[8,9]. While available data collectively reveal a largely anoxic Ediacaran ocean with spatially heterogeneous and temporally dynamic redox conditions[9,10] related to episodic incursion of oxygenated waters[11], the tempo and magnitude of oceanic oxygenation remain uncertain.

It has been suggested that a Neoproterozoic oxygenation event (NOE) occurred following the Tonian, during which oxygen accumulated and ventilated the deep oceans[2]. Multiple oceanic oxygenation events (OOEs) during the Ediacaran have been inferred on the basis of various geochemical proxies, including carbon and sulfur isotopes[1,5,12], Fe speciation data[13], nitrogen isotopes[14], uranium isotopes[15], molybdenum isotopes[16], thallium isotopes[17,18], chromium isotopes[19], and redox-sensitive element enrichments[7,11]. The scope of these OOEs is debated, with effects either extending into the deep ocean[7,11,14] or limited to continental shelves[9,16,19,20]. However, both hypotheses seem to contradict existing evidence of widespread anoxia in Ediacaran oceans[8,10,21]. A high-frequency ocean-redox oscillation model has been proposed, in which brief oxic interludes occurred within a largely euxinic ocean[18,22,23]. This scenario might have permitted the emergence and diversification of early animals such as those in the Lantian Biota[22,24]. However, direct evidence of high-frequency redox fluctuations is lacking.

Here, we report the mineralogy, morphology, and distribution of distinctive early diagenetic sulfide rosettes consisting of pyrite and marcasite that are preserved in shallow-marine phosphorite-carbonate successions of the lower Doushantuo Formation at Weng'an, South China (Fig. 1). Combined with carbon-, sulfur- and iron-isotope data, the Doushantuo pyrite-marcasite associations reveal a complex diagenetic history controlled by redox variation in oceanic bottom waters and sediment porewaters. These data provide evidence for incursions of oxygenated waters into the sediment, supporting the occurrence of high-frequency oxygenation events on the Ediacaran shelf seafloor during a critical period in the early evolution of complex life.

Geological setting and samples. The Ediacaran Doushantuo Formation is widely distributed in South China (Fig. 1a). Paleogeographic studies of the Doushantuo successions have shown deposition of carbonate and siliciclastic rocks on a northwestern platform that evolved to distal sediments of slope and basinal facies to the southeast (Fig. 1a). The Doushantuo strata vary in thickness from 40 m to 300 m and often show rapid lateral lithofacies variations[25–27]. In the intrashelf Jiulongwan section, typical Doushantuo successions are exposed and are subdivided into four members based on lithostratigraphy and chemostratigraphy (Fig. 1c)[25–28]. The depositional age of the Doushantuo Formation in the Yangtze Gorges area has been well constrained as between 635 and 551 Ma by U-Pb dating of zircons from tuff layers[29,30].

At Weng'an, the Doushantuo Formation is a phosphorite-carbonate-dominated succession with minor occurrences of siliciclastic beds near its base (Fig. 1b, c). It is generally subdivided into five lithological units[31], consisting of a basal 'cap carbonate' unit (unit 1), a lower, banded phosphorite unit (unit 2, LPB), a massive dolostone unit (unit 3), an upper phosphate-rich unit (UPB) composed of carbonaceous phosphorites (unit 4 A) and laminated phosphorites (unit 4B), and an uppermost unit of intraclastic dolostones (unit 5). The UPB is an important fossil Lagerstätte that features exceptionally preserved phosphatized spheroids that have been interpreted as animal embryo fossils[31–35]. The Unit 2 phosphorites have a banded or laminated structure (Supplementary Fig. 1), consist of various types of phosphatic grains[36,37], contain abundant cyanobacterial microfossils[37], and accumulated in an offshore-shelf setting under transgressive conditions[36,37].

Although the entire Doushantuo Formation at Weng'an can be correlated with that in the Yangtze Gorges area, the ages of the five units (particularly of Unit 4 that contains the Weng'an Biota) remain controversial. Previous studies have yielded Pb-Pb isochron ages of 599 ± 4 Ma[38] and 576 ± 26 Ma[39] for Unit 4B and suggested that the age of the Weng'an Biota is ca. 600 Ma, but the reliability of these ages have been questioned[29]. Alternatively, the exposure surface atop Unit 3 (Fig. 1c) has been related to the Gaskiers glaciation, which implies that the Weng'an Biota is probably younger than 580 Ma[29]. Based on litho- and biostratigraphic data, Unit 2 at Weng'an can be well correlated with the lower Member II shale-carbonate interval in the Yangtze Gorges area. This, along with a newly obtained Re-Os age of 587.2 ± 3.6 Ma from the middle Member II in the Yangtze Gorges area[40], document that the Weng'an Biota is probably not older than 587 Ma, whereas Unit 2 (the sampled interval of this study) were deposited between 632.5 Ma[29] and 587.2 Ma[40].

A total of 51 phosphorite samples were collected from drillcores and an outcrop section (Fig. 1c, Supplementary Fig. 1) spanning Unit 2 of the Doushantuo Formation in the study area. In total 45 of the 51 samples come from drillcores ZK115, ZK208, ZK430, ZK1202 (Fig. 1b; see Supplementary Note 1 for details), with an average sampling density of about one sample per meter (Fig. 1c).

Results

Occurrences of sulfide rosettes. Unit 2 of the Doushantuo Formation typically contains abundant (1–5%) sub-millimeter-sized aggregates of sulfides (Figs. 2–4) that are associated with banded or laminated granular phosphorite (Fig. 2a–e, Supplementary Fig. 1b–d). The sulfide aggregates commonly form millimeter-thick, bedding-parallel laminae in granular phosphorites (Fig. 2a, b, Supplementary Fig. 2), and appear to be more abundant in dolomite-rich layers (Fig. 2c, d). Compactional deformation of laminae around large sulfide aggregates (Fig. 2e) indicates that the latter precipitated prior to significant sediment compaction. Dissolution of dolomite matrix, phosphatic peloid grains and glauconite and replacement by sulfide aggregates are commonly observed (Fig. 2e–h), whereas all these phases are cemented or partly replaced by a second-generation dolomite of early diagenetic or burial diagenetic origin (Fig. 2i).

Mineralogy and paragenesis. Approximately 90% of the Doushantuo sulfide aggregates are rosettes primarily consisting of pyrite and marcasite (Fig. 3) that are hereafter termed "pyrite-marcasite rosettes" (PMRs). The PMRs vary in size from 7 μm to 1 mm (Supplementary Table 1) but are all similar in structure and composition (Supplementary Fig. 3). Well-developed PMRs are typically 100 to 200 μm across, consist of a framboidal or irregular pyrite nucleus and a cortex composed of radiating marcasite blades, and have an outermost pyrite rim (Fig. 3a, d, f, Supplementary Fig. 3), although incomplete rosettes are also present (Fig. 4, Supplementary Fig. 4). Rare occurrences of composite PMRs are also observed, with at least two rosettes enclosed by a final pyrite rim (Fig. 4j, Supplementary Fig. 3e, f). In addition to pyrite and marcasite, the PMRs exhibit a complex mineralogy characterized by the ubiquitous presence of quartz and organic matter in the cortex (Fig. 3a, e–h) and local occurrence of barite

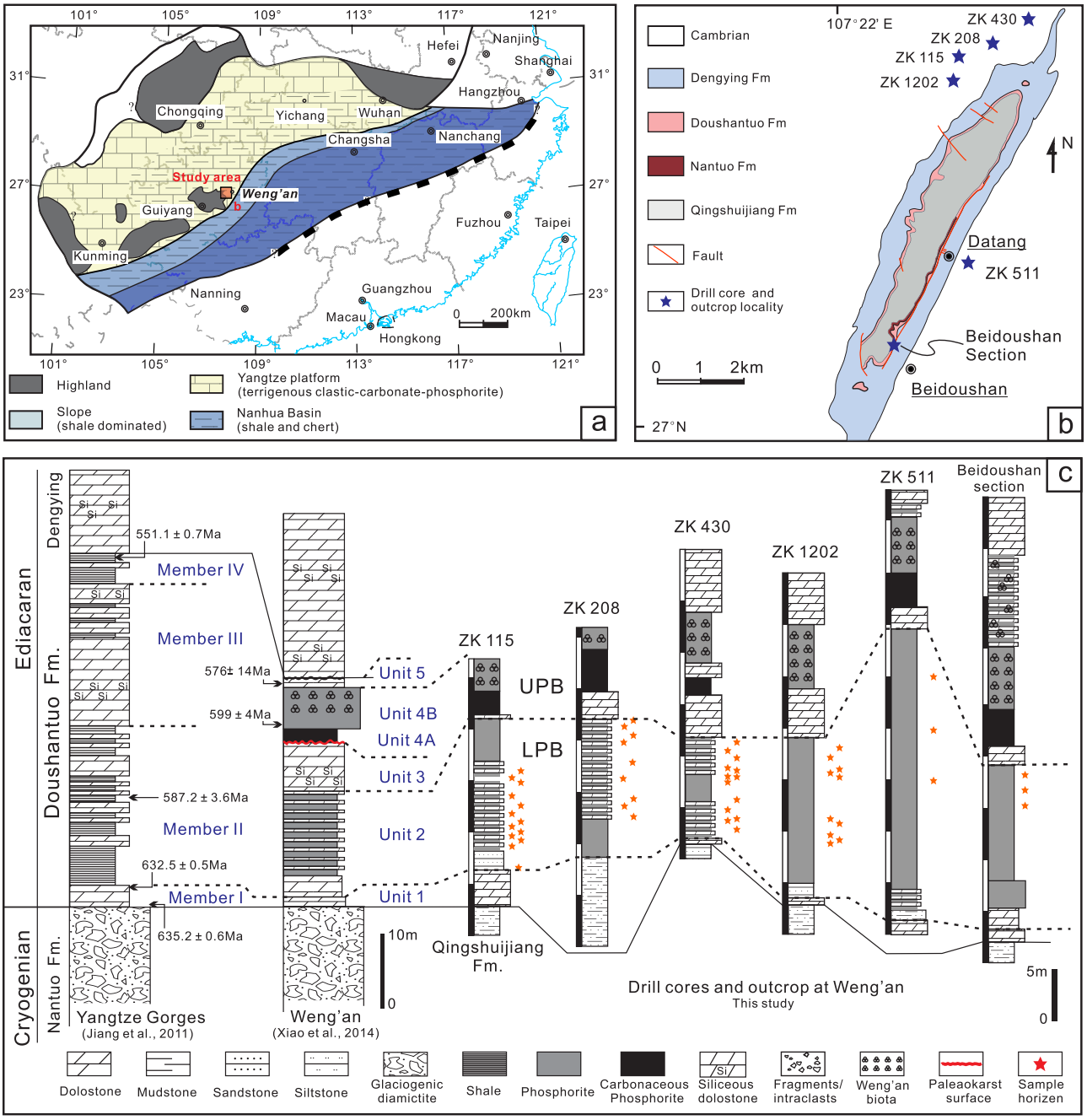

Fig. 1 Geological maps and stratigraphic columns. a Generalized paleogeographic map of the Yangtze Platform during the Doushantuo deposition (modified after ref. [25]). **b** Simplified geological map of the study area; **c** Stratigraphic columns of the Doushantuo Formation in the Yangtze Gorges and Weng'an areas. UPB upper phosphorite bed, LPB lower phosphorite bed.

(Fig. 3f). Raman spectra document a low to moderate thermal maturity for the organic matter (Fig. 3f), with a calculated peak heating temperature of 161–215 °C (Supplementary Table 2). Trace amounts of rutile and anatase are also present in some PMRs (Supplementary Fig. 4f).

The nuclei of PMRs generally consist of pyrite framboids (Fig. 4e–g) or irregular pyrite lumps (Figs. 3d, 4h, i) <50 μm in size. In other cases, the PMR nuclei are larger aggregates of pyrite exhibiting a poikilitic texture, frequently with irregular shapes that may be due to corrosion (Fig. 3a–c). Clusters of pyrite framboids with variable degrees of recrystallization and structural degradation are commonly observed (Supplementary Fig. 4), likely representing the precursor of the larger PMR nuclei. Considering PMRs as the product of an integrated sulfide growth history, a variety of intermediate states can be recognized. These include: (1) pyrite framboids and an early pyrite rim generation (Fig. 4a, b); (2) irregular pyrite aggregates (Fig. 4c) likely as a result of recrystallization of multiple framboids followed by partial dissolution; (3) pyrite-marcasite rosettes composed of pyrite nuclei that are surrounded by marcasite blades and quartz (Figs. 3a, 4d–h); and (4) complete PMRs with pyrite nucleus, marcasite blades, and an outermost pyrite rim (Figs. 3d, 4i, j). The best-developed sulfide rosettes thus record a five-stage growth history (Fig. 4): (I) nucleation and growth of pyrite framboids, (II) concentric overgrowth of an early generation of pyrite rim, (III) aggregation, dissolution and recrystallization of the pyrite framboid and rim, (IV) radial growth of marcasite blades, and (V) formation of a final generation of pyrite rim.

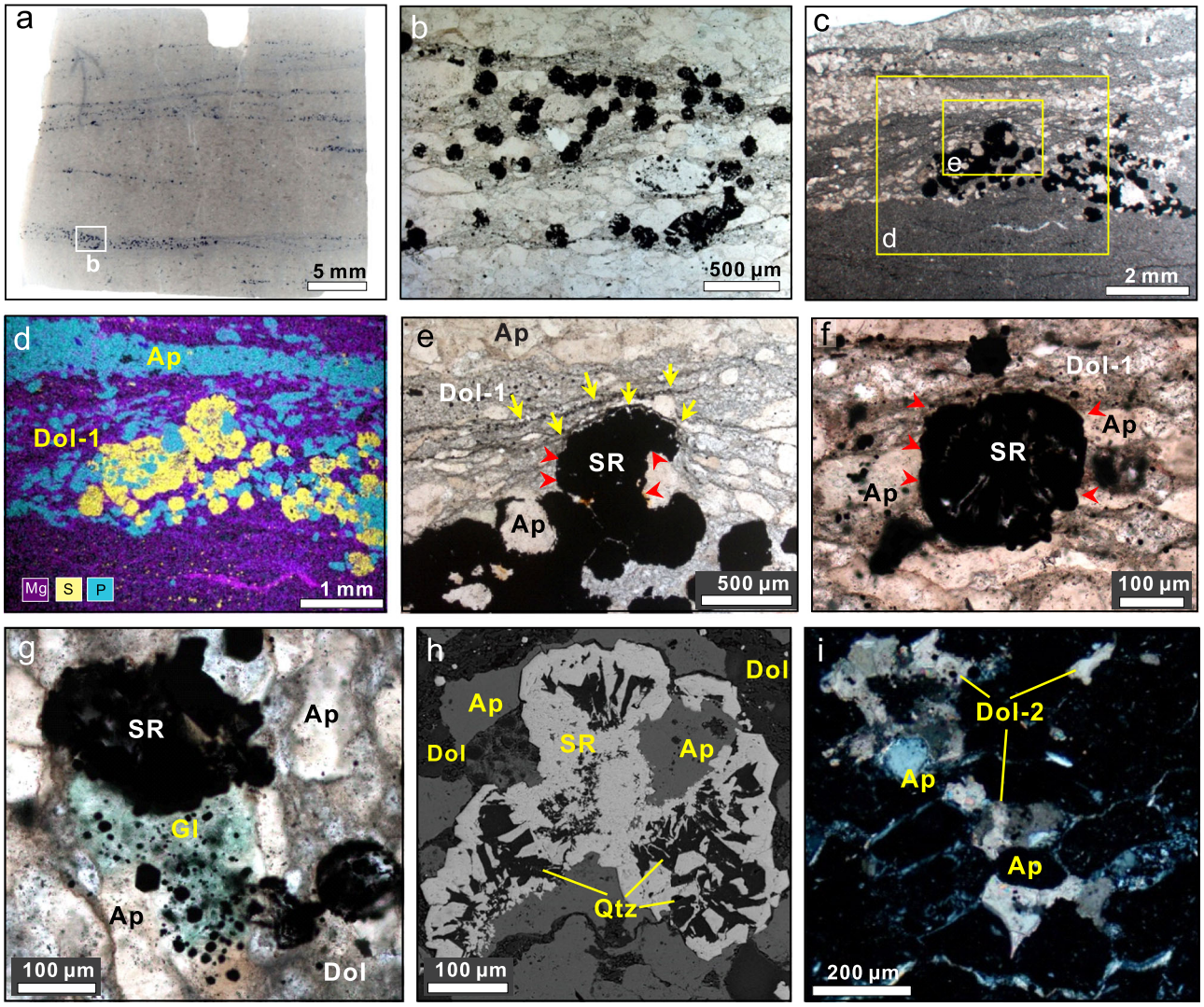

Fig. 2 Occurrences of sulfide rosettes and their paragenetic context. a Bedding-parallel distribution of sulfides (opaque) in a granular phosphorite. **b** Close-up of the area marked in (**a**) showing local abundance of sulfide rosettes. **c**–**e** A phosphatic dolostone composed of dolomite matrix (Dol-1), phosphate (Ap) peloids and abundant sulfide rosettes. **d** Overlayered elemental distribution of Mg, S, and P for the area marked in **c**. **e** Close-up of the area outlined in **c**, showing that sedimentary lamina (arrows) drape around opaque sulfide rosettes (SR) and partial dissolution of phosphate peloid grains (Ap) and dolomite (arrowheads). **f** A sulfide rosette crosscutting phosphate grains and dolomite matrix (arrowheads). **g**, **h** Dissolution of phosphate grains, dolomite and glauconite (Gl) and replacement by sulfide rosettes. Note the presence of quartz (Qtz) in the rosettes. **i** A second generation, highly birefringent dolomite (Dol-2) cementing and replacing isotropic phosphatic granules (Ap). **a** Thin section scan; **b**, **c**, **e**–**g** transmitted plane-polarized light image; **d** elemental map by EDS; **h** secondary electron image; **i**, transmitted light image, crossed polars.

Carbon, oxygen, sulfur and iron isotopes. Carbonate C and O isotopes were determined for 16 microdrilled powder samples of PMR-containing dolomite-rich layers (Supplementary Fig. 5). Their $\delta^{13}C_{carb}$ and $\delta^{18}O_{carb}$ compositions range from −2.55‰ to +1.74‰ (mean +0.16‰) and −7.37‰ to −0.24‰ (mean −3.14‰), respectively (Supplementary Table 3). Except for two extreme values (−2.55‰ and +1.74‰), the $\delta^{13}C_{carb}$ profile shows small fluctuations around 0‰. Strong covariation of $\delta^{13}C_{carb}$ and $\delta^{18}O_{carb}$ is observed for the full sample suite ($R^2 = 0.58$, $p < 0.01$, Supplementary Fig. 5).

S and Fe isotopes were measured in situ on relatively large marcasite blades, pyrite nuclei and pyrite rims in representative PMRs, as well as on some associated sulfide aggregates (Fig. 4k, l, Supplementary Figs. 6–8). The $\delta^{34}S$ ranges of pyrite nuclei and marcasite blades (cortex) are −25.15‰ to −14.36‰ (mean −18.65‰) and −27.86‰ to −15.21‰ (mean −20.66‰), respectively (Fig. 5, Supplementary Table 4). In contrast, the outermost pyrite rims exhibit systematically heavier $\delta^{34}S$ ranging between −9.55‰ and +0.14‰ with a mean of −5.76‰ (Fig. 5). Within individual PMRs, the marcasite cortex tends to yield lower $\delta^{34}S$ than the pyrite nucleus with few exceptions (Fig. 4k, Supplementary Figs. 6–8).

$\delta^{56}Fe$ varies from −0.11‰ to +1.45‰ (mean +0.66‰) for marcasite cortices and from +0.17‰ to +1.09‰ (mean +0.31‰) for pyrite nuclei (Supplementary Table 5). Large inter-grain variation is observed, with $\delta^{56}Fe$ values ranging between +0.07‰ and +1.45‰ at the millimeter scale (Supplementary Fig. 6). It is interesting to note that, within individual PMRs, the marcasite cortex tends to have lighter $\delta^{56}Fe$ than the pyrite nucleus, with a fractionation ($\triangle^{56}Fe_{marc\text{-}py}$) of −0.56‰ to −0.42‰ (Fig. 4l).

Stratigraphic variation of sulfide mineralogy and size. At Weng'an, PMRs are observed only in Unit 2 of the Doushantuo Formation. Detailed mapping and measurements of PMR size in

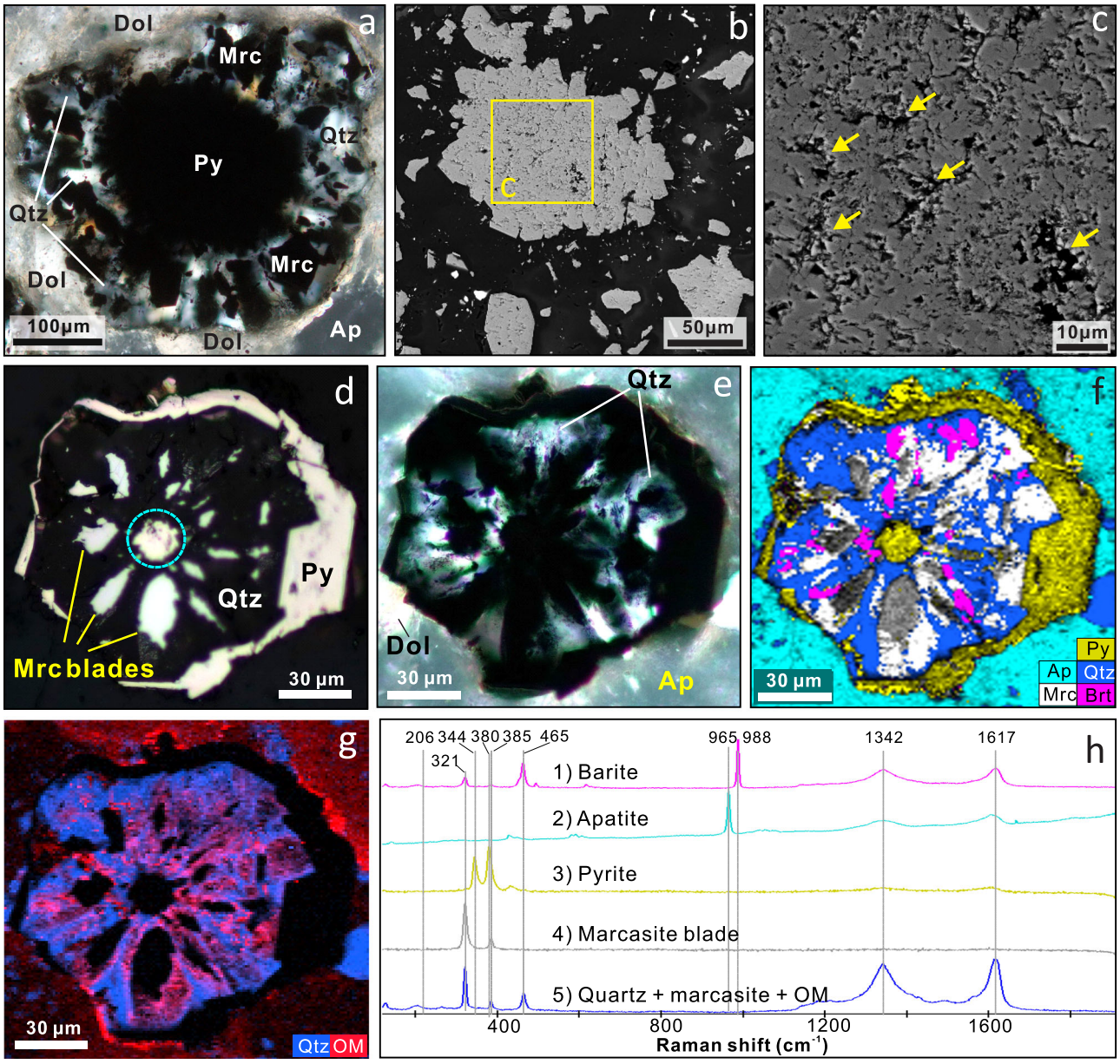

Fig. 3 Texture and mineralogy of typical pyrite-marcasite rosettes (PMRs). a A PMR composed of a relatively large pyrite (Py) nucleus and a cortex composed of intergrown quartz (Qtz) and radiating marcasite (Mrc) blades. **b**, **c** Close-up of the PMR nucleus showing irregular shape (**b**) and poikilitic internal texture (**c**) as a result of corrosion. **d**–**g** A PMR consisting of a small, irregular pyrite nucleus (circled in **d**), a cortex of intergrown quartz (Qtz) and radiating marcasite (Mrc) blades, and a pyrite rim (Py). **f** Raman image of the PMR showing the distribution of apatite (Ap), quartz, pyrite, marcasite and barite (Brt). **g** Raman image showing the presence of organic matter (OM) in the quartz of the cortex and in the surrounding apatite. Note the intergrowth of quartz and marcasite (**f**) and ubiquitous presence of organic matter in quartz and apatite (**g**). **h** Raman spectra of various phases. **a**, **e** Transmitted light image, crossed polars; **b**, **c** backscattered electron image; **d** reflected light image.

three drillcores revealed similar stratigraphic patterns. Pyrite framboids are most common in the middle and upper parts of Doushantuo Unit 2, whereas marcasite blades are most common in the lower part of the unit (Fig. 6). Quartz is present in all rosettes containing marcasite, consistent with a close spatial association between these two phases (Fig. 3a, e, f). The size of pyrite framboids ranges from 2 μm to 20 μm, without an apparent stratigraphic trend. The size of the rosettes, however, is generally greater in the lower part of Unit 2 (100–500 μm) than in its upper part (10–50 μm), with a maximum size of about 1 mm at 1.5 to 3 m above the unit base (Fig. 6, Supplementary Table 1). The ratio of marcasite blade length to pyrite nucleus diameter (Mrc/Py) shows higher values in the lower part of Unit 2 than in its upper part, mirroring the pattern of stratigraphic variation in rosette size.

Discussion

Marcasite (FeS_2, orthorhombic), although less well known than its polymorph pyrite (FeS_2, cubic), has been reported from various sedimentary successions and metal deposits (Supplementary Table 6). The relative scarcity of marcasite compared with pyrite in the geological record may stem from two factors: (1) marcasite formation requires acidic conditions (pH = ~4–5)[41,42], whereas neutral-alkaline environments (pH = ~7–8) favor pyrite formation[43], and (2) marcasite is a metastable mineral that

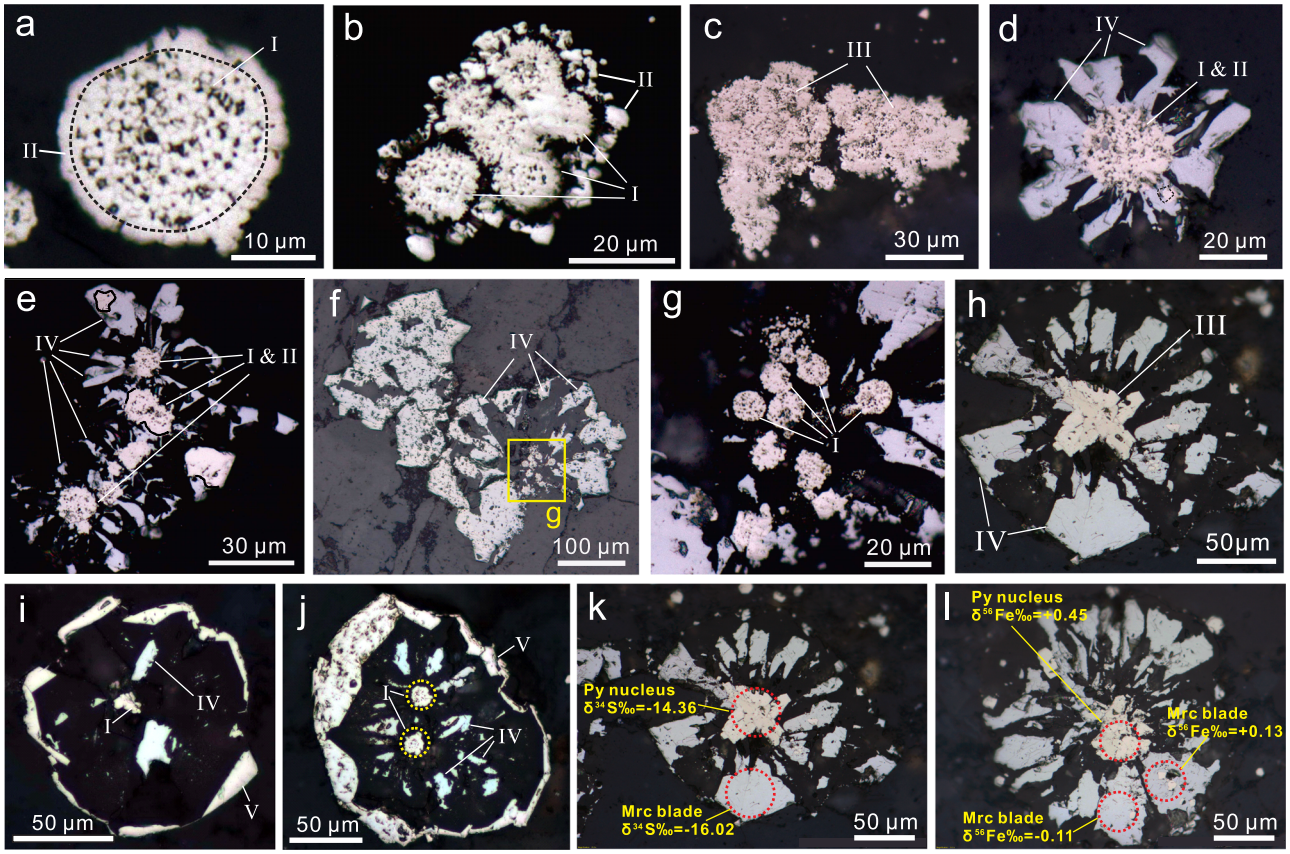

Fig. 4 Paragenetic sequence of the sulfide rosettes. a, **b** Pyrite framboid(s) (I) enclosed within a pyrite rim (II). **c** Irregular pyrite aggregates (III) showing poikilitic texture. **d**–**j** PMRs with various textures. **d** A PMR with a spheroidal pyrite nucleus (recrystallized framboid) and radiating marcasite blades (IV). **e**, **f** Aggregates of PMRs with spheroidal pyrite nuclei. **g** Close-up of the area outlined in **f** showing multiple framboids in the center of the PMR. **h** A PMR with a nucleus of irregular pyrite. **i**, **j** Complete PMRs consisting of an irregular pyrite nucleus or two framboid-like pyrite nuclei (I), radiating marcasite blades (IV) and an outer rim of pyrite (V). **k**, **l** Representative PMRs analyzed for S and Fe isotopes and their $\delta^{34}S$ values and $d^{56}Fe$ values. All images were taken under the reflected light. Five generations of sulfide growths are identified: (I) pyrite framboid; (II) pyrite rim I; (III) pyrite aggregates (degraded framboids); (IV) marcasite blades; (V) pyrite rim II.

readily converts to pyrite at temperatures greater than 400 °C during heating experiments[44], and that has an estimated lifespan of ~1.5 Myr at burial temperatures of 300 °C[45]. The preservation of marcasite in the Doushantuo Formation of the Weng'an area is thus consistent with the relatively low peak burial temperatures (161 to 215 °C) derived from the Raman spectra of organic matter (Supplementary Table 2). The Doushantuo phosphorites, along with the ~1.1-Ga Bijaygar Shale of the Vindhyan Supergroup in India[46] and banded iron formation of the ~2.7-Ga Hunter Mine Group in Canada[47], are rare examples of marcasite-bearing Precambrian strata. In addition, the Cryogenian Datangpo Formation of South China contains fibrous Fe-oxide coronas surrounding a pyrite nucleus and enclosed by a pyrite rim, possibly representing oxidized pseudomorphs after marcasite[48].

Marcasite formation has been reported in various modern environments, including marine hydrothermal systems[49], methane seeps[50], and waterlogged acidic soils in coastal settings[51]. In the hydrothermal environment, pyrite and marcasite often co-occur with metalliferous minerals containing gold/silver[52], copper[53], lead/zinc[54], and uranium[55] (Supplementary Table 6). Despite extensive mapping using optical microscopy, SEM-EDS and Raman spectroscopy, no metal-bearing hydrothermal minerals have been identified in the Doushantuo samples, which accumulated in shallow-marine settings that are unlikely to have been significantly influenced by hydrothermal activity. Moreover, the low S-isotopic compositions of the pyrite nuclei (mean $\delta^{34}S$ −18.65‰) and marcasite (mean $\delta^{34}S$ −20.66‰) are inconsistent with hydrothermal influences, which typically result in sulfides with $\delta^{34}S > -10‰$[56]. These considerations make a hydrothermal origin for the Doushantuo marcasite unlikely.

Texturally similar sulfide rosettes have been reported from modern methane seep sediments, typically consisting of a framboidal core and radial pyrite overgrowths[50,57]. In such seep environments, pyrite formed by sulfate-driven anoxic methane oxidation (SD-AOM) exhibits highly variable and frequently elevated $\delta^{34}S$ compositions (up to +115‰)[57]. In the Doushantuo Formation, extremely ^{13}C-depleted calcite-cement $\delta^{13}C$ compositions have been reported from the Member I cap dolostone (to −48‰)[58], the base of Member II (to −38.1‰)[59], and the uppermost part of Member II (to −34‰)[60], which have been invoked as evidence for the methane signals[61]. During anoxic methane oxidation (AOM), two mole-equivalents of alkalinity are generated per mole of DIC produced, leading to an increase in porewater pH[62,63] that is expected to favor the formation of pyrite over marcasite. This is consistent with the scarcity of documented occurrences of marcasite crystals in modern seep sediments[57], although high-resolution transmission electron microscopy has revealed the presence of <10-nm-thick marcasite layers in some AOM-related pyrites[50]. The absence of ^{34}S-enriched sulfides and extremely ^{13}C-depleted carbonates in the present study (Supplementary Tables 3–4) further excludes SD-AOM as a plausible origin for the Doushantuo PMRs.

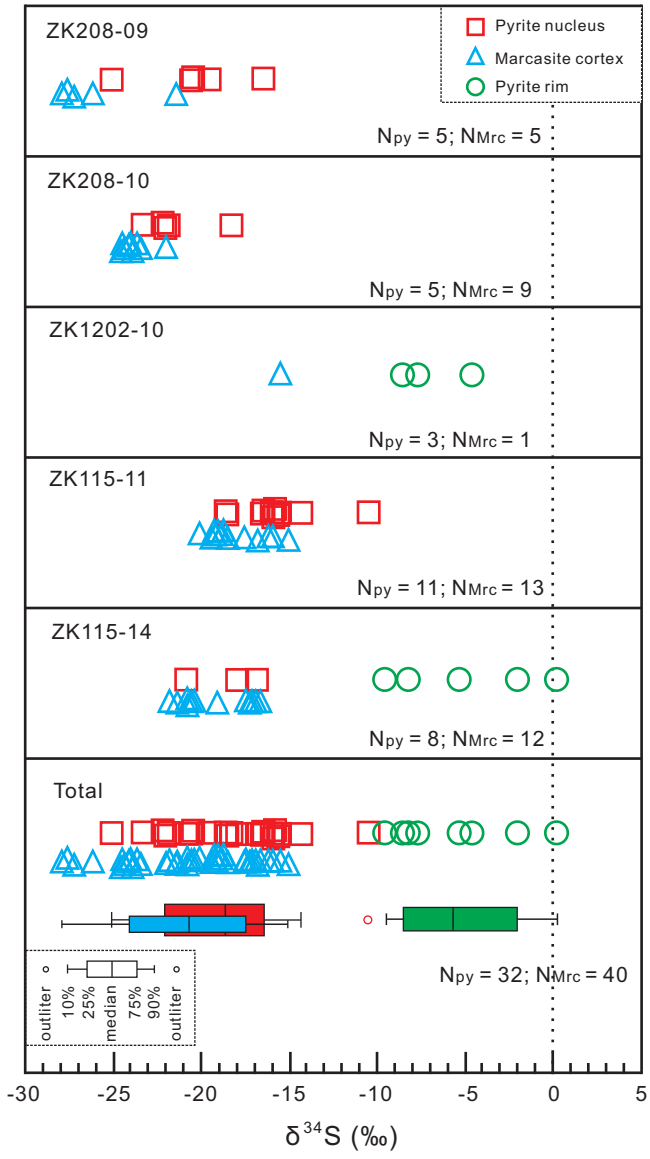

Fig. 5 Distributions of pyrite and marcasite $\delta^{34}S$ of nucleus, cortex, and rim of PMRs. The $\delta^{34}S$ values of pyrite nucleus (red box) and marcasite cortex (blue box) have similar ranges (generally < -15‰) although the latter tend to be slightly lower, whereas the outermost pyrite rims exhibit systematically higher $\delta^{34}S$ (> -10‰, green box).

Experimental studies have demonstrated that the formation of marcasite requires low pH (4 to 5)[41,42], whereas a literature survey of pH in modern surficial sediments indicates an absence of pH values below 6.4[46]. Instead, downward diffusion of oxidizing bottom waters, resulting in oxidation of pyrite (Eq. 1)[64] in the sediments, can generate a decline of porewater pH to <5, which allows marcasite precipitation[46,65].

$$FeS_2 + \frac{7}{2}O_2\,(aq) + H_2O \rightarrow Fe^{2+} + 2SO_4^{2-} + 2H^+ \qquad (1)$$

Indeed, pyrite oxidation and porewater acidification in the Doushantuo Formation are supported by the generally irregular shapes and corrosional features of the PMR nuclei (Fig. 3b, d), as well as the widespread dissolution textures observed from the phosphatic grains and dolomite matrix around the PMRs (Fig. 2e–h). The ubiquitous intergrowth of marcasite and quartz in the cortices (Fig. 3) is consistent with rapid co-precipitation of these phases under acidic conditions created by pyrite oxidation. Rapid formation of the marcasite-quartz cortex would ensure preservation of small amounts of barite (Fig. 3f) that possibly have formed simultaneously with marcasite and quartz or as a residual phase prior to the formation of pyrite nuclei. The diverse morphological and textural features of PMR nuclei and associated sulfide aggregates (Fig. 4, Supplementary Figs. 3–4) in the Doushantuo Formation can also be explained by repeated dissolution and reprecipitation of sulfides during early diagenesis.

Our sulfur and iron isotopic results also support the oxidation of pyrite nuclei and followed growth of marcasite blades during early diagenesis. The uniformly negative $\delta^{34}S$ values for the pyrite nuclei of PMRs (–25.15‰ to –14.36‰, mean –18.65‰) are consistent with microbial sulfate reduction in a semi-open system, such as in diagenetic porewaters near the sediment-water interface[66,67]. Subsequent partial oxidation of these pyrites would produce sulfate without an evident S isotope fractionation, as documented by pyrite oxidation experiments[68], and thus would not affect the $\delta^{34}S$ composition of the sulfate reservoir. This explains the similar range of negative $\delta^{34}S$ values for marcasite (–27.86‰ to –15.21‰, mean –20.66‰, Fig. 5 and Supplementary Figs. 6–8), supporting their early diagenetic origin. In contrast, the remarkably heavier $\delta^{34}S$ signals of the outer pyrite rims (–9.55‰ to +0.14‰, mean –5.76‰) suggest a Rayleigh fractionation in closed environments upon burial of the sediments[66,67].

Fe isotopes has been commonly used to track redox transformations of Fe-bearing species, because Fe-isotopic fractionation can result from redox changes between aqueous Fe(II) and Fe(III) species and adsorption of Fe(II) onto Fe(III)-oxides, producing $Fe(II)_{aq}$ with $\delta^{56}Fe$ values lower than that of Fe(III) species at equilibrium[69,70]. In our study, the lighter $\delta^{56}Fe$ composition of the marcasite cortex (–0.01‰ to +0.03‰) relative to the pyrite nucleus (+0.45‰) of the same PMR (Fig. 4i) is consistent with oxidative dissolution of pyrite and rapid precipitation of ^{56}Fe-depleted marcasite, although this remains to be tested with a larger dataset.

The formation of PMRs prior to sediment compaction in the lower Doushantuo Formation suggests that most of the above-mentioned processes likely have taken place rapidly during early diagenesis. A similar scenario has been reported in pyrite-marcasite associations in black shales ranging in age from the Mesoproterozoic to Cretaceous[46,65]. In these sediments, euhedral or tabular μm-size marcasite grains occur in close association with corroded pyrite framboids and quartz, and they sometimes form sulfide rosettes with a pyrite nucleus and radial-bladed marcasite overgrowths that resemble the Doushantuo rosettes[46]. As in the Doushantuo Formation, the differential compaction of sediment laminae around sulfide rosettes in these black shales is evidence for an early diagenetic origin. Marcasite-pyrite intergrowth textures have also been reported from sedimentary sequences at the Permian-Triassic Boundary (PTB), which were interpreted as evidence of a sudden acidification of late Permian seawater[71,72]. Although some of these textures are similar to the Doushantuo PMRs, the PTB marcasites typically have highly depleted $\delta^{34}S$ values (ca. –50‰) and were probably formed in open porewaters connected to an unlimited marine sulfate reservoir[72], which is unlikely the case for the Doushantuo Formation.

Based on our petrographic observations and isotopic data, we propose a redox-pH model (Fig. 7) to explain the formation of various sulfide rosettes in the Doushantuo Formation. This model includes four early diagenetic stages:

1. Formation of initial pyrite nucleus. Microbial sulfate reduction resulted in the formation of pyrite framboids in an anoxic-suboxic water column and subsequent pyrite overgrowths in the surficial dolomitic phosphorite sediment, leading to aggregation of some framboids.

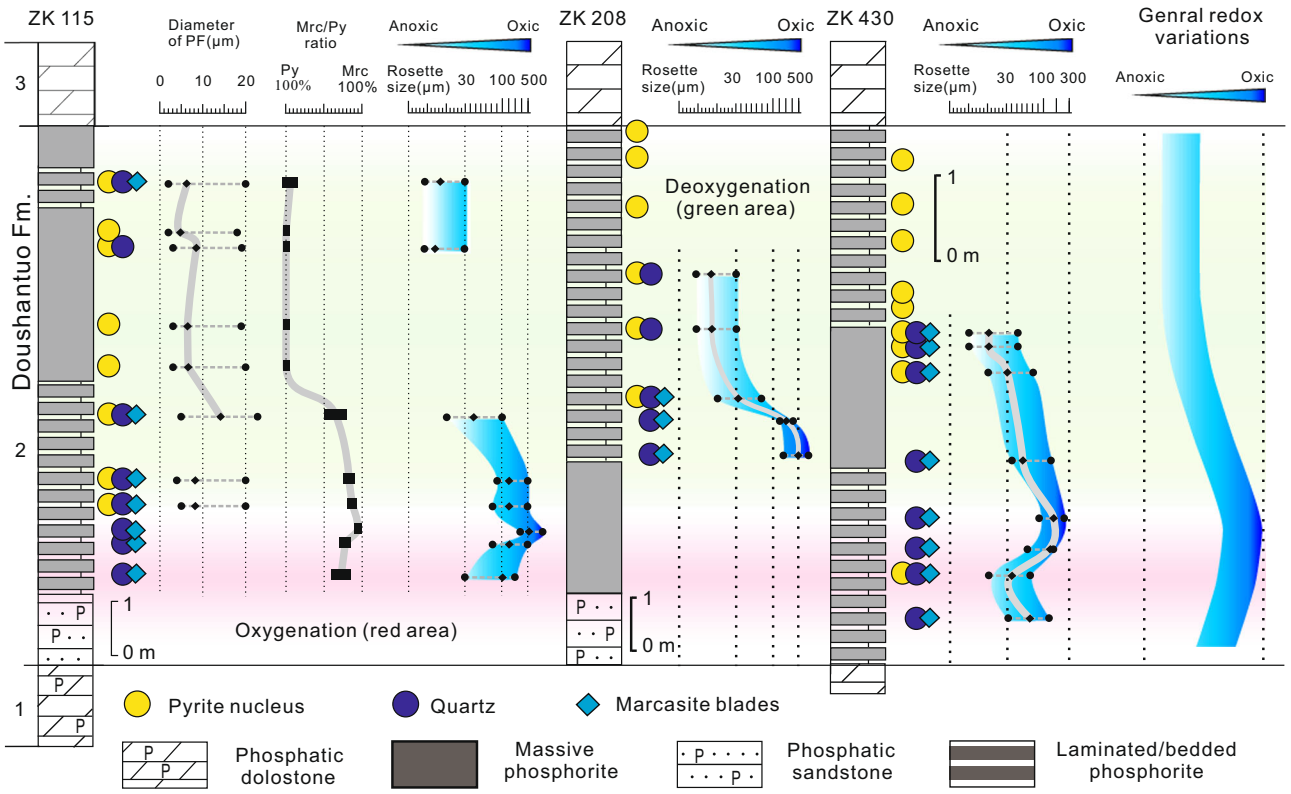

Fig. 6 Stratigraphic variations of sulfide mineralogy and inferred porewater redox conditions. Mrc/Py ratio denotes the ratio of marcasite blade length to pyrite nucleus diameter. Relative redox conditions of different horizons are estimated based on the size ranges of rosettes, which show a general decreasing trend upsection but with fluctuations near the base.

2. Alternating dissolution and precipitation of pyrite nucleus. Downward diffusion of oxidizing bottom waters caused corrosion and oxidative dissolution of previously formed pyrite framboids, dolomite matrix and phosphatic grains, as well as production of sulfuric acid and a consequent decline of porewater pH. Oxidation of organic matter during this stage might have also contributed to porewater acidification, but to a lesser extent. The heterogeneity of O_2 levels in the porewaters resulted in variably oxidized/corroded textures of pyrite grains. Repeated transient oxygen incursions resulted in alternating pyrite dissolution and precipitation, yielding larger pyrite nuclei up to several hundred microns in size.
3. Co-precipitation of marcasite and quartz. The acidic conditions produced by pyrite oxidation promoted rapid co-precipitation of marcasite and quartz around the remnant pyrite nucleus, forming the cortex of the PMR that entombed remains of other phases such as organic matter and barite. Stages 2 and 3 are represented by the following reactions (Eq. 2)[41,42]:

$$\mathrm{FeS_2\,(Py) + O_2 \xrightarrow{ph>6} Fe^{2+} + S_xO_y + H^+ \xrightarrow{OM} Fe^{2+}} \\ \mathrm{+ H_nS_m + H^+ \xrightarrow{ph<5} FeS_2\,(Mrc)} \quad (2)$$

where S_xO_y and H_nS_m refer to sulfoxy and sulfide intermediates, respectively.
4. Formation of outer pyrite rim. With the exhaustion of H^+, the porewater became neutral/alkaline and pyrite precipitation was favored, leading to growth of a final pyrite rim. This stage appears to have taken place in a deeper, less-open porewater system, as indicated by the much higher $\delta^{34}S$ values of the outer pyrite rims, a result of Rayleigh fractionation of porewater sulfate. Typical PMRs and other sulfide rosettes may form in microenvironments with slightly variable porewater chemistry.

A key variable in this series of diagenetic stages is dissolved O_2, which controlled the formation and alteration of pyrite nuclei and other precipitates by creating heterogenous porewater conditions in terms of Eh and pH. The pyrite nuclei tend to be framboids or small aggregates when dissolution was dominant (Fig. 4d–g, j) but may be larger lumps when alternating dissolution and precipitation occurred (Fig. 3a). If bottom waters were not sufficiently oxidizing to enable porewater pH to fall to ≤ 5, pyrite lumps without marcasite blades formed (Fig. 4c). In contrast, when porewater pH fell to ≤ 5, marcasite blades grew (Figs. 3, 4d–i, and Supplementary Fig. 3). Following this reasoning, we infer that the growth of marcasite and the size of PMRs were controlled mainly by the availability of O_2 in the porewater. The occurrence of pyrite lumps and remarkably large rosettes in the lower part of Doushantuo Unit 2 (Fig. 6, Supplementary Table 1) may record a period of bottom-water oxygenation. The upper part of Unit 2 is characterized by much smaller rosettes and the eventual disappearance of pyrite lumps and marcasite blades, signifying a shift to less oxidizing bottom waters (Fig. 6). This shift of benthic redox conditions is further supported by the relatively higher abundance of pyrite framboids in the upper part of Unit 2.

In the Doushantuo study section, the partial preservation of pyrite nuclei, barite and organic matter imply that marcasite formation was a product of repeated small-scale, transient oxidation events. Since the formation of pyrite nuclei requires sulfidic porewaters and marcasite growth requires acidic conditions linked to oxidation of early diagenetic pyrite by incursions of O_2,

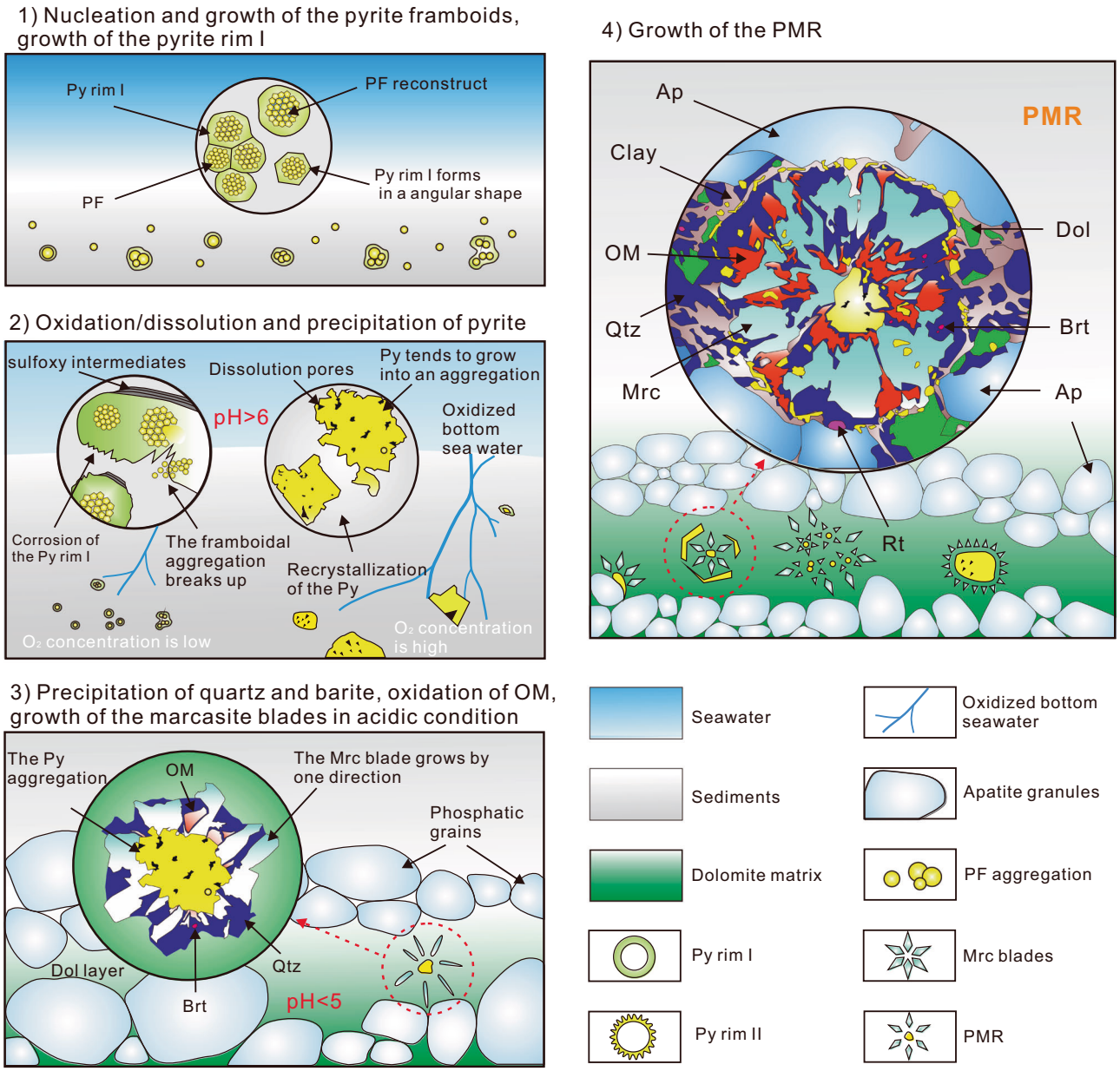

Fig. 7 A redox-pH model envisaging the formation of Doushantuo PMRs. Typical PMRs are formed through the four stages, whereas heterogeneous porewater conditions (Eh and pH) in a semi-open system could have resulted in different paths of mineral precipitation and transformation and led to the formation of sulfide rosettes with various morphologies and mineralogies.

the presence of PMRs in multiple layers of the lower Doushantuo Formation points to repeated incursions of oxygenated bottom waters into Ediacaran shelf sediments. Frequent fluctuations of bottom-water and diagenetic porewater redox states may have also promoted the formation and transformation of Fe-bearing authigenic phases such as glauconite[73] and phosphosiderite[74] in the Doushantuo Formation. Similar redox models such as "poikiloredox conditions[20,23]" or brief oxic episodes[22,67] have been proposed to explain the contradiction between the long-term anoxic oceanic environments (indicated by iron species data[23,75] and oxic conditions evidenced by enrichment of redox-sensitive trace elements[7,11] and diversification of macroscopic eukaryotes such as those in the Lantian Biota[22,24]. The occurrence of pyrite-marcasite associations reported in this study provides direct evidence for high-frequency oxygenation of Early Ediacaran continental shelves. Such oxygenation episodes in an otherwise anoxic environment are likely to have promoted the contemporaneous emergence and diversification of complex metazoans such as the Weng'an Biota[31] and Lantian Biota[22,24]. Moreover, pyrite-marcasite associations in unmetamorphosed sedimentary rocks, especially when coupled with Fe-S isotope data, constitute a promising mineralogical proxy for paleoredox reconstructions.

Methods

Optical microscopy. Petrographic studies were performed on 30-μm-thick, polished thin-sections with a Nikon LV100 POL or a Zeiss Axio Scope microscope at China University of Geosciences–Wuhan, and with an Olympus BX51 microscope at University College London. Preliminary discriminations between pyrite and marcasite were based on their color in the reflected light mode. In total, the diameters of 4231 sulfide targets in thin section were measured and the ratio of marcasite blade length to

pyrite nucleus diameter calculated, as summarized in Supplementary Table 1.

Confocal micro-Raman spectroscopy. Micro-Raman spectroscopic imaging was performed at the London Center for Nanotechnology, UCL, and at the State Key Laboratory of Biogeology and Environmental Geology, China University of Geosciences–Wuhan with a WITec alpha 300 R system equipped with a 532-nm laser with output power maintained at 3 ~ 8 mW. A 50-μm-diameter optic fiber was selected as a compromise between confocality and signal-to-noise ratio, and a 600 grove/mm grating was used to provide a large bandwidth of 4000 cm^{-1} and a spectral resolution of 4 cm^{-1}. The analyses were performed at least 0.5 μm below the sample surface to rule out potential contamination on the sample surface. Raman hyperspectral images of mineral associations were generated by mapping the main peak intensities (or unique peaks) for specific minerals using the WITec Project data processing software; the peaks include those distinct for OM (~1334 $cm^{-1}$and ~1625 cm^{-1}), dolomite (~ 1100 cm^{-1}), barite (~ 987 cm^{-1}), apatite (~ 967 cm^{-1}), rutile (~609 cm^{-1}), quartz (~467 cm^{-1}), pyrite (~ 379 cm^{-1}), marcasite (~ 322 cm^{-1}), and anatase (~ 141 cm^{-1}). All Raman peak positions were read directly from measured average spectra calculated from representative regions with high signal-to-noise and after background removal. Minerals are shown coded in different colors according to their characteristic peaks. Deconvolution of Raman peaks of OM (D1, D2, D3, D4, and G) was performed using linear combinations of the Lorentz function. Temperatures are estimated after Kouketsu et al.[76] according to the applicable range of temperatures.

Scanning electron microscopy and energy dispersive spectroscopy (SEM-EDS). Scanning electron microscopy (SEM) was carried out using a TESCAN VEGA 3 SEM at the State Key Laboratory of Biogeology and Environmental Geology, China University of Geosciences–Wuhan. Analyses were performed on uncoated polished thin sections under a vacuum pressure of 10^{-3} mbar in the sample chamber and with a 0.25 nA electron beam accelerated at 15–20 keV. X-rays were collected on an electronically-cooled Oxford Instrument AztecOne EDS detector to generate spectra or elemental images.

Carbon and oxygen isotope analysis. Oxygen and carbon isotopic composition ($\delta^{18}O$ and $\delta^{13}C$) of 17 samples were analyzed at the State Key Laboratory of Geological Processes and Mineral Resources, China University of Geosciences–Wuhan. Powders were microdrilled from dolomite-rich layers with a hand-held dental carbide microdrill. About 60–100 μg of the microdrilled powder was analyzed using a Kiel IV Carbonate Device (100% H3PO4 for 220 s at 70 °C) connected to a Finnigan MAT 253 mass spectrometer[77]. For both procedures, every nine samples including a random repeated sample were followed by a standard. All of the C- and O-isotope results are reported relative to the Vienna Pee Dee Belemnite (VPDB) standard with a precision better than ± 0.1‰ based on duplicate analyses of Chinese national standards (GBW04416 and GBW04417).

In situ S isotope analysis. In situ sulfur isotope analyses of sulfide were performed on a Neptune Plus MC-ICP-MS (Thermo Fisher Scientific, Bremen, Germany) equipped with an NWR FemtoUC femtosecond system (New Wave Research, Fremont, CA, U.S.A.) at the state Key Laboratory of Geological Processes and Mineral Resources, China University of Geosciences–Wuhan. The single spot ablation mode was used with a spot size of 40 μm, a pulse frequency of 4 Hz and a laser fluence of ~2.5 J/cm^2. A standard-sample bracketing method (SSB) was employed to correct for instrumental mass fractionation. A pyrite standard PPP-1 ($\delta^{34}S_{V\text{-}CDT} = +5.40 \pm 0.16‰$) was used as external standard to correct the mass fractionation of S isotopes for various sulfide samples. In addition, several in-house reference standards, including the pyrrhotite YP136 ($\delta^{34}S_{V\text{-}CDT} = +1.50 \pm 0.30‰$)[78] and the chalcopyrite JGZ-87 ($\delta^{34}S_{V\text{-}CDT} = +5.50 \pm 0.23‰$), were analyzed repeatedly as unknowns to verify the accuracy of the calibration method. Because matrix-matched standards for marcasite are scarce, in practice a pyrite standard is commonly used to calibrate the sulfur isotope ratios of marcasite[79,80]. This method has proven reliable by a recent study during SIMS analysis[81], which yielded in situ $\delta^{34}S$ values for marcasite consistent with the result determined using gas source isotope ratio mass spectrometry. Data reduction for LA-MC-ICP-MS analysis was conducted for a total of 72 targets using the ISO-Compass software[82].

In situ Fe isotope analysis. In situ Fe isotopes of sulfides were analyzed by fs-LA-MC-ICP-MS at the Institute of Mineralogy, Leibniz University Hannover (Germany), using a high-mass-resolution MC-ICP-MS (Thermo-Finnigan Neptune Plus) connected to a femtosecond laser ablation system. The LA system was built in-house based on a Spectra-Physics Solstice femtosecond (fs) laser operating in the deep UV at 194 nm, with a pulse energy of 70 μJ from a regenerative amplified system pumped with 500 Hz. The ablation cell was modified from New Wave LUV 266[83], and the ablation spot size was ca. 40 μm in diameter. The fs-LA-MC-ICP-MS Fe isotope measurements were performed at a high mass resolution ($M/\Delta M \approx 9000$, 5–95% peak side width definition) to resolve molecular interferences of argon nitrides and argon oxides on Fe isotopes[84]. Additionally, a Ni reference solution (NIST SRM 986, 5 ppm Ni in 0.5 M HNO_3 solution) was added to the plasma along with the ablation aerosol, in order to monitor external mass bias using the measured Ni isotope ratios[85] and to maintain a "wet" plasma condition[86]. Measured Fe isotope compositions are reported using delta notation, and $\delta^{56}Fe$ values are given as deviation in per mille (‰) from the composition of reference material IRMM-14 (Institute of Reference Materials and Measurements standard 014), as expressed as follows:

$$\delta^{56}Fe = \left\{ \left[\left({}^{56}Fe/{}^{54}Fe \right)_{sample} / \left({}^{56}Fe/{}^{54}Fe \right)_{IRMM-14} \right] - 1 \right\} \times 1000 \quad (3)$$

The IRMM-14 reference standard was measured after each sample for drift monitoring. Applying a similar procedure, a high accuracy of ≤0.1‰ has been achieved for $\delta^{56}Fe$ in a variety of materials including sulfides which showed that a matrix-matched bracketing standard is not required, and that all these materials can be measured accurately against a metal standard[83]. In our analytical sessions, we used an internal secondary pure Fe reference material (PURATRONIC, Johnson Matthey, lot no. FE495007IF2, 99.995% Fe), and we reproduced $\delta^{56}Fe$ values within ±0.05‰. The 10 spots analysed in the same session (Supplementary Table 5) yield a linear regression of $\delta^{57}Fe = 1.475 \times \delta^{56}Fe$ ($R^2 = 0.98$, $p < 0.001$), and the obtained slope is in good agreement with the mass-dependent fractionation ratio of 1.475[87]. More details about the equipment setup and analytical procedure are available in Horn et al. [83] and Oeser et al. [85].

Data availability

Supplementary Tables 1–5 are available at the figshare database https://doi.org/10.6084/m9.figshare.24224737.

Received: 10 January 2023; Accepted: 27 October 2023;
Published online: 22 November 2023

References

1. Fike, D. A., Grotzinger, J. P., Pratt, L. M. & Summons, R. E. Oxidation of the Ediacaran ocean. *Nature* **444**, 744–747 (2006).
2. Shields-Zhou, G. & Och, L. The case for a Neoproterozoic Oxygenation Event: geochemical evidence and biological consequences. *GSA Today* **21**, 4–11 (2011).
3. Xiao, S. & Laflamme, M. On the eve of animal radiation: phylogeny, ecology and evolution of the Ediacara biota. *Trends Ecol. Evol.* **24**, 31–40 (2009).
4. Lenton, T. M., Boyle, R. A., Poulton, S. W., Shields-Zhou, G. A. & Butterfield, N. J. Co-evolution of eukaryotes and ocean oxygenation in the Neoproterozoic Era. *Nature Geoscience* **7**, 257–265 (2014).
5. Mcfadden, K. A. et al. Pulsed oxidation and biological evolution in the Ediacaran Doushantuo Formation. *Proc. Natl Acad. Sci. USA* **105**, 3197–3202 (2008).
6. Rooney, A. D., Cantine, M. D., Bergmann, K. D., Gómez-Pérez, I. & Strauss, J. V. Calibrating the coevolution of Ediacaran life and environment. *Proc. Natl Acad. Sci. USA* **117**, 16824–16830 (2020).
7. Sahoo, S. K. et al. Ocean oxygenation in the wake of the Marinoan glaciation. *Nature* **489**, 546–549 (2012).
8. Lyons, T. W., Diamond, C. W., Planavsky, N. J., Reinhard, C. T. & Li, C. Oxygenation, life, and the planetary system during Earth's middle history: an overview. *Astrobiology* **21**, 906–923 (2021).
9. Li, C., Shi, W., Cheng, M., Jin, C. & Algeo, T. J. The redox structure of Ediacaran and early Cambrian oceans and its controls. *Sci. Bull.* **65**, 2141–2149 (2020).
10. Li, C. et al. A stratified redox model for the Ediacaran ocean. *Science* **328**, 80–83 (2010).
11. Sahoo, S. K. et al. Oceanic oxygenation events in the anoxic Ediacaran ocean. *Geobiology* **14**, 457–468 (2016).
12. Shi, W. et al. Sulfur isotope evidence for transient marine-shelf oxidation during the Ediacaran Shuram Excursion. *Geology* **46**, 267–270 (2018).
13. Canfield, D. E., Poulton, S. W. & Narbonne, G. M. Late-Neoproterozoic deep-ocean oxygenation and the rise of animal life. *Science* **315**, 92–95 (2007).
14. Wang, X., Jiang, G., Shi, X., Peng, Y. & Morales, D. C. Nitrogen isotope constraints on the early Ediacaran ocean redox structure. *Geochim. Cosmochim. Acta* **240**, 220–235 (2018).
15. Kendall, B. et al. Uranium and molybdenum isotope evidence for an episode of widespread ocean oxygenation during the late Ediacaran Period. *Geochim. Cosmochim. Acta* **156**, 173–193 (2015).
16. Yang, X., Long, X., Li, J., Dong, Y. & Zhao, B. Mo isotopic response to the end of Neoproterozoic Marinoan glaciation: Evidence from a sedimentary profile in South China. *Precambrian Res.* **339**, 105609 (2020).
17. Fan, H. et al. Constraining oceanic oxygenation during the Shuram excursion in South China using thallium isotopes. *Geobiology* **18**, 348–365 (2020).
18. Ostrander, C. M. et al. Thallium isotope ratios in shales from South China and northwestern Canada suggest widespread O_2 accumulation in marine bottom waters was an uncommon occurrence during the Ediacaran Period. *Chem. Geol.* **557**, 119856 (2020).
19. Xu, D. et al. Chromium isotope evidence for oxygenation events in the Ediacaran ocean. *Geochim. Cosmochim. Acta* **323**, 258–275 (2022).
20. Li, C., Cheng, M., Zhu, M. & Lyons, T. W. Heterogeneous and dynamic marine shelf oxygenation and coupled early animal evolution. *Emerg. Top. Life Sci.* **2**, 279–288 (2018).
21. Tostevin, R. et al. Uranium isotope evidence for an expansion of anoxia in terminal Ediacaran oceans. *Earth Planetary Sci. Lett.* **506**, 104–112 (2019).
22. Wang, W. et al. Integrated carbon, sulfur, and nitrogen isotope chemostratigraphy of the Ediacaran Lantian Formation in South China: Spatial gradient, ocean redox oscillation, and fossil distribution. *Geobiology* **15**, 552–571 (2017).
23. Jin, C. et al. Highly heterogeneous "poikiloredox" conditions in the early Ediacaran Yangtze Sea. *Precambrian Res.* **31**, 157–166 (2018).
24. Yang, C. et al. Implications for Ediacaran biological evolution from the ca. 602 Ma Lantian biota in China. *Geology* **50**, 562–566 (2022).
25. Zhu, M., Zhang, J. & Yang, A. Integrated Ediacaran (Sinian) chronostratigraphy of South China. *Palaeogeogr. Palaeoclimatol. Palaeoecol.* **254**, 7–61 (2007).
26. Jiang, G., Shi, X., Zhang, S., Wang, Y. & Xiao, S. Stratigraphy and paleogeography of the Ediacaran Doushantuo Formation (ca. 635–551 Ma) in South China. *Gondwana Res.* **19**, 831–849 (2011).
27. Zhu, M. et al. Carbon isotope chemostratigraphy and sedimentary facies evolution of the Ediacaran Doushantuo Formation in western Hubei, South China. *Precambrian Res.* **225**, 7–28 (2013).
28. Zhou, C. & Xiao, S. Ediacaran $\delta^{13}C$ chemostratigraphy of South China. *Chem. Geol.* **237**, 89–108 (2007).
29. Condon, D. et al. U-Pb ages from the neoproterozoic Doushantuo Formation. *China.* **308**, 95–98 (2005).
30. Zhang, S., Jiang, G. & Han, Y. The age of the Nantuo Formation and Nantuo glaciation in South China. *Terra Nova* **20**, 289–294 (2008).
31. Xiao, S., Zhou, C., Liu, P., Wang, D. & Yuan, X. Phosphatized acanthomorphic acritarchs and related microfossils from the Ediacaran Doushantuo Formation at Weng'an (South China) and their implications for biostratigraphic correlation. *Journal of Paleontology* **88**, 1–67 (2014).
32. Xiao, S., Zhang, Y. & Knoll, A. H. Three-dimensional preservation of algae and animal embryos in a Neoproterozoic phosphorite. *Nature* **391**, 553–558 (1998).
33. Xiao, S. & Knoll, A. H. Phosphatized animal embryos from the Neoproterozoic Doushantuo formation at Weng'an, Guizhou, South China. *J. Paleontol.* **74**, 767–788 (2000).
34. Chen, L., Xiao, S., Pang, K., Zhou, C. & Yuan, X. Cell differentiation and germ–soma separation in Ediacaran animal embryo-like fossils. *Nature* **516**, 238–241 (2014).
35. Yin, Z. et al. Sponge grade body fossil with cellular resolution dating 60 Myr before the Cambrian. *Proc. Natl Acad. Sci. USA* **112**, E1453–E1460 (2015).
36. Zhang, Y., Pufahl, P. K., Du, Y., Chen, G. & Yu, W. Economic phosphorite from the Ediacaran Doushantuo Formation, South China, and the Neoproterozoic-Cambrian Phosphogenic Event. *Sedimentary Geol.* **388**, 1–19 (2019).
37. Jiao, L. et al. Integrated stratigraphy and mineralogy of the Doushantuo Formation in Weng'an, South China, and implications for Ediacaran phosphogenesis. *J. Earth Sci.* (2023).
38. Barfod, G. H. et al. New Lu–Hf and Pb–Pb age constraints on the earliest animal fossils. *Earth Planet. Sci. Lett.* **201**, 203–212 (2002).
39. Chen, D. F., Dong, W. Q., Zhu, B. Q. & Chen, X. P. Pb–Pb ages of Neoproterozoic Doushantuo phosphorites in South China: constraints on early metazoan evolution and glaciation events. *Precambrian Res.* **132**, 123–132 (2004).
40. Yang, C. et al. The tempo of Ediacaran evolution. *Sci. Adv.* **7**, eabi9643 (2021).
41. Mckibben, M. A. & Barnes, H. L. Oxidation of pyrite in low temperature acidic solutions: rate laws and surface textures. *Geochim. Cosmochim. Acta* **50**, 1509–1520 (1986).
42. Schoonen, M. A. A. & Barnes, H. L. Reactions forming pyrite and marcasite from solution: II. Via FeS precursors below 100 °C. *Geochim. Cosmochim. Acta* **55**, 1505–1514 (1991).
43. Rickard, D., Schoonen, M. A. A. & Luther, G. W. Chemistry of iron sulfides in sedimentary environments. In: *Geochemical Transformations of Sedimentary Sulfur*, ACS Symposium Series, Vol. 612, pp. 168–193 (1995).
44. Fleet, M. E. Structure aspects of the marcasite-pyrite transformation. *Can. Mineral.* **10**, 225–231 (1970).
45. Yao, X. et al. The mechanism and kinetics of the transformation from marcasite to pyrite: in situ and ex situ experiments and geological implications. *Contrib. Mineral. Petrol.* **175**, 1–25 (2020).
46. Schieber, J. Marcasite in black shales—A mineral proxy for oxygenated bottom waters and intermittent oxidation of carbonaceous muds. *J. Sediment. Res.* **81**, 447–458 (2011).
47. Mueller, W. U. & Mortensen, J. K. Age constraints and characteristics of subaqueous volcanic construction, the Archean Hunter Mine Group, Abitibi greenstone belt. *Precambrian Res.* **115**, 119–152 (2002).
48. Cui, H. et al. Questioning the biogenicity of Neoproterozoic superheavy pyrite by SIMS. *Am. Mineral.* **103**, 1362–1400 (2018).
49. Maginn, E. J., Little, C. T. S., Herrington, R. J. & Mills, R. A. Sulphide mineralisation in the deep sea hydrothermal vent polychaete, *Alvinella pompejana*: implications for fossil preservation. *Mar. Geol.* **181**, 337–356 (2002).
50. Zhang, M. et al. Morphology and formation mechanism of pyrite induced by the anaerobic oxidation of methane from the continental slope of the NE South China Sea. *J. Asian Earth Sci.* **92**, 293–301 (2014).
51. Bush, R. T., Mcgrath, R. & Sullivan, L. A. Occurrence of marcasite in an organic-rich Holocene estuarine mud. *Soil Res.* **42**, 617–621 (2004).
52. Yilmaz, H., Oyman, T., Arehart, G. B., Colakoglu, A. R. & Billor, Z. Low-sulfidation type Au–Ag mineralization at Bergama, Izmir, Turkey. *Ore Geol. Rev.* **32**, 81–124 (2007).
53. Franchini, M. et al. Trace metals in pyrite and marcasite from the Agua Rica porphyry-high sulfidation epithermal deposit, Catamarca, Argentina: textural features and metal zoning at the porphyry to epithermal transition. *Ore Geol. Rev.* **66**, 366–387 (2015).
54. Decrée, S. et al. Pb-Zn mineralization in a Miocene regional extensional context: the case of the Sidi Driss and the Douahria ore deposits (Nefza mining district, northern Tunisia). *Ore Geol. Rev.* **34**, 285–303 (2008).
55. Min, M., Jia, C., Wang, J., Wei, G. & Fayek, M. Mineral paragenesis and textures associated with sandstone-hosted roll-front uranium deposits, NW China. *Ore Geol. Rev.* **26**, 51–69 (2005).

56. Hutchison, W., Finch, A. A. & Boyce, A. J. The sulfur isotope evolution of magmatic hydrothermal fluids: insights into ore-forming processes. *Geochim. Cosmochim. Acta* **288**, 176–198 (2020).
57. Lin, Z. et al. How sulfate-driven anaerobic oxidation of methane affects the sulfur isotopic composition of pyrite: A SIMS study from the South China Sea. *Chem. Geol.* **440**, 26–41 (2016).
58. Wang, J., Jiang, G., Xiao, S., Li, Q. & Wei, Q. Carbon isotope evidence for widespread methane seeps in the ca. 635 Ma Doushantuo cap carbonate in south China. *Geology* **36**, 347–350 (2008).
59. Zhou, C., Guan, C., Cui, H., Ouyang, Q. & Wang, W. Methane-derived authigenic carbonate from the lower Doushantuo Formation of South China: implications for seawater sulfate concentration and global carbon cycle in the early Ediacaran ocean. *Palaeogeogr. Palaeoclimatol. Palaeoecol.* **461**, 145–155 (2016).
60. Cui, H. et al. Phosphogenesis associated with the Shuram Excursion: petrographic and geochemical observations from the Ediacaran Doushantuo Formation of South China. *Sediment. Geol.* **341**, 134–146 (2016).
61. Kennedy, M. J., Christie-Blick, N. & Sohl, L. E. Are Proterozoic cap carbonates and isotopic excursions a record of gas hydrate destabilization following Earth's coldest intervals? *Geology* **29**, 443–446 (2001).
62. Lu, R., Wallmann, K. & Aloisi, G. Numerical modeling of carbonate crust formation at cold vent sites: signi¢cance for £uid and methane budgets and chemosynthetic biological communities. *Earth Planetary Sci. Lett.* **221**, 337–353 (2004).
63. Jourabchi, P., Cappellen, P. V. & Regnier, P. Quantitative interpretation of pH distributions in aquatic sediments: a reaction-transport modeling approach. *Am. J. Sci.* **305**, 919–956 (2005).
64. Chandra, A. P. & Gerson, A. R. The mechanisms of pyrite oxidation and leaching: a fundamental perspective. *Surface Science Reports* **65**, 293–315 (2010).
65. Schieber, J. Oxidation of detrital pyrite as a cause for marcasite formation in marine lag deposits from the Devonian of the eastern US. *Deep Sea Res. Part II: Top. Stud. Oceanogr.* **54**, 1312–1326 (2007).
66. Machel, H. G. Bacterial and thermochemical sulfate reduction in diagenetic settings—old and new insights. *Sediment. Geol.* **140**, 143–175 (2001).
67. Wang, W., Hu, Y., Muscente, A. D., Cui, H. & Zhou, C. Revisiting Ediacaran sulfur isotope chemostratigraphy with in situ nanoSIMS analysis of sedimentary pyrite. *Geology* **49**, 611–616 (2021).
68. Balci, N., Shanks, W. C. III, Mayer, B. & Mandernack, K. W. Oxygen and sulfur isotope systematics of sulfate produced by bacterial and abiotic oxidation of pyrite. *Geochim. Cosmochim. Acta* **71**, 3796–3811 (2007).
69. Mansor, M. & Fantle, M. S. A novel framework for interpreting pyrite-based Fe isotope records of the past. *Geochim. Cosmochim. Acta* **253**, 39–62 (2019).
70. Guilbaud, R., Butler, I. B. & Ellam, R. M. Abiotic pyrite formation produces a large Fe isotope fractionation. *Science* **332**, 1548–1551 (2011).
71. Lounejeva, E. et al. Marcasite at the Permian-Triassic transition: a potential indicator of hydrosphere acidification. In: *Large Igneous Provinces* (eds Ernst R. E., Dickson A. J., Bekker A.) (2021).
72. Li, R. et al. A rapid onset of ocean acidification associated with the end-Permian mass extinction. *Glob. Planet. Change* **225**, 104130 (2023).
73. Algabri, M., She, Z., Jiao, L., Papineau, D. & Li, C. Apatite-glaucony association in the Ediacaran Doushantuo Formation, South China and implications for marine redox conditions. *Precambrian Res.* **347**, 105842 (2020).
74. Schwid, M. F., Xiao, S., Hiatt, E. E., Fang, Y. & Nolan, M. R. Iron phosphate in the Ediacaran Doushantuo Formation of South China: a previously undocumented marine phosphate sink. *Palaeogeogr. Palaeoclimatol. Palaeoecol.* **560**, 109993 (2020).
75. Sperling, E. A. et al. Statistical analysis of iron geochemical data suggests limited late Proterozoic oxygenation. *Nature* **523**, 451–454 (2015).
76. Kouketsu, Y. et al. A new approach to develop the Raman carbonaceous material geothermometer for low-grade metamorphism using peak width. *Island Arc.* **23**, 33–50 (2014).
77. Chang, B. et al. Episodic massive release of methane during the mid-Cretaceous greenhouse. *GSA Bull.* **134**, 2958–2970 (2022).
78. Li, R., Xia, X., Yang, S., Chen, H. & Yang, Q. Off-mount calibration and one new potential pyrrhotite reference material for sulfur isotope measurement by secondary ion mass spectrometry. *Geostand. Geoanal. Res.* **43**, 177–187 (2019).
79. Wu, Y.-F. et al. Ore-forming processes of the Daqiao epizonal orogenic gold deposit, West Qinling Orogen, China: constraints from textures, trace elements, and sulfur isotopes of pyrite and marcasite, and raman spectroscopy of carbonaceous material. *Econ. Geol.* **113**, 1093–1132 (2018).
80. Jowett, E. C., Roth, T., Rydzewski, A. & Oszczepalski, S. "Background" $\delta^{34}S$ values of Kupferschiefer sulphides in Poland: pyrite-marcasite nodules. *Mineralium Deposita* **26**, 89–98 (1991).
81. Li, R., Wang, X.-L., Guan, Y., Gu, J. & Tian, L.-L. The feasibility of using a pyrite standard to calibrate the sulfur isotope ratio of marcasite during SIMS analysis. *J. Anal. Atom. Spectrom.* **38**, 1016–1020 (2023).
82. Zhang, W., Hu, Z. & Liu, Y. Iso-Compass: new freeware software for isotopic data reduction of LA-MC-ICP-MS. *J. Anal. Atomic Spectrom.* **35**, 1087–1096 (2020).
83. Horn, I., Blanckenburg, F. V., Schoenberg, R., Steinhoefel, G. & Markl, G. In situ iron isotope ratio determination using UV-femtosecond laser ablation with application to hydrothermal ore formation processes. *Geochim. Cosmochim. Acta* **70**, 3677–3688 (2006).
84. Weyer, S. & Schwieters, J. B. High precision Fe isotope measurements with high mass resolution MC-ICPMS. *Int. J. Mass Spectrom.* **226**, 355–368 (2003).
85. Oeser, M., Weyer, S., Horn, I. & Schuth, S. High-precision Fe and Mg isotope ratios of silicate reference glasses determined in situ by femtosecond LA-MC-ICP-MS and by solution nebulisation MC-ICP-MS. *Geostand. Geoanal. Res.* **38**, 311–328 (2014).
86. Zheng, X. Y., Beard, B. L. & Johnson, C. M. Assessment of matrix effects associated with Fe isotope analysis using 266 nm femtosecond and 193 nm nanosecond laser ablation multi-collector inductively coupled plasma mass spectrometry. *J. Anal. Atom. Spectrometry* **33**, 68–83 (2018).
87. Dauphas, N. & Rouxel, O. Mass spectrometry and natural variations of iron isotopes. *Mass Spectrometry Reviews* **25**, 515–550 (2006).

Acknowledgements

This work was financially supported by National Natural Science Foundation of China (grant# 41825019, 42130208 and 41821001), the National Key Research and Development Program of China (2023YFC2906601 and 2022YFF0800102). Z.S. and L.J. thank Ingo Horn (Hannover) for help with Fe isotope analysis, Jiasheng Wang and Meng Cheng for inspiring discussions, and Yaguan Zhang, Guoyong Chen, Qun Chen and Chao Deng for help with fieldwork. Z.S. acknowledges support from the Bureau of Geology and Mineral Resources of Guizhou Province for sampling permission in their core library.

Author contributions

Z.S. designed the research, D.P. and C.L. helped to improve it. L.J. wrote the manuscript with important contributions from all co-authors. Z.S. and L.J. conducted the petrographic analyses, SEM-EDS, Raman spectroscopy, and S isotope measurements. C.Z. performed the Fe isotope analysis. T.J.A., C.L., G.L., M.D., and K.C. helped with review and editing.

Competing interests

The authors declare no competing interests.

Additional information

Supplementary information The online version contains supplementary material available at https://doi.org/10.1038/s43247-023-01080-1.

Correspondence and requests for materials should be addressed to Zhenbing She.

Peer review information *Communications Earth & Environment* thanks the anonymous reviewers for their contribution to the peer review of this work. Primary Handling Editors: Xiaoming Liu and Joe Aslin. A peer review file is available.

Reprints and permission information is available at http://www.nature.com/reprints

Publisher's note Springer Nature remains neutral with regard to jurisdictional claims in published maps and institutional affiliations.